



Characterization of a unique polysaccharide monooxygenase from the plant pathogen *Magnaporthe oryzae*

Alejandra Martinez-D'Alto^a , Xia Yan^b, Tyler C. Detomasi^{c1} , Richard I. Sayler^a , William C. Thomas^a , Nicholas J. Talbot^b , and Michael A. Marletta^{a,c,d,2}

Contributed by Michael A. Marletta; received September 8, 2022; accepted January 12, 2023; reviewed by J. Martin Bollinger, James W. Kronstad, and Brian G. Miller

Blast disease in cereal plants is caused by the fungus *Magnaporthe oryzae* and accounts for a significant loss in food crops. At the outset of infection, expression of a putative polysaccharide monooxygenase (*MoPMO9A*) is increased. *MoPMO9A* contains a catalytic domain predicted to act on cellulose and a carbohydrate-binding domain that binds chitin. A sequence similarity network of the *MoPMO9A* family AA9 showed that 220 of the 223 sequences in the *MoPMO9A*-containing cluster of sequences have a conserved unannotated region with no assigned function. Expression and purification of the full length and two *MoPMO9A* truncations, one containing the catalytic domain and the domain of unknown function (DUF) and one with only the catalytic domain, were carried out. In contrast to other AA9 polysaccharide monooxygenases (PMOs), *MoPMO9A* is not active on cellulose but showed activity on cereal-derived mixed (1→3, 1→4)- β -D-glucans (MBG). Moreover, the DUF is required for activity. *MoPMO9A* exhibits activity consistent with C4 oxidation of the polysaccharide and can utilize either oxygen or hydrogen peroxide as a cosubstrate. It contains a predicted 3-dimensional fold characteristic of other PMOs. The DUF is predicted to form a coiled-coil with six absolutely conserved cysteines acting as a zipper between the two α -helices. *MoPMO9A* substrate specificity and domain architecture are different from previously characterized AA9 PMOs. The results, including a gene ontology analysis, support a role for *MoPMO9A* in MBG degradation during plant infection. Consistent with this analysis, deletion of *MoPMO9A* results in reduced pathogenicity.

polysaccharide monooxygenase | *Magnaporthe oryzae* | blast disease

Polysaccharide monooxygenases (PMOs), also known as lytic PMOs, are Cu-dependent secreted enzymes that facilitate polysaccharide degradation. These enzymes hydroxylate the glycosidic linkage of polymeric carbohydrate substrates such as cellulose (1) and chitin (2). Since their discovery, over 16,000 putative PMOs have been identified across nearly all kingdoms of life (3–5). PMOs play a major role in nutrient acquisition, and expression increases in the presence of substrates (6, 7). PMOs are widespread in the genomes of both bacteria and filamentous fungi, with some organisms encoding over twenty PMOs (8). This multiplicity within an individual organism, combined with their widespread presence across phyla, suggests that PMOs are likely to play roles beyond that of biomass degradation (9, 10). Indeed, roles in development (11, 12), endosymbiosis (9, 13–15), and pathogenesis (16–19) have been reported.

The ascomycete *Magnaporthe oryzae* is the plant pathogen that causes blast disease in cereal crops (20). Rice blast disease is by far the most devastating rice disease, causing a loss of 10 to 35% of the world's annual harvest, and is found wherever rice is grown (21, 22). During the initial stage of infection, *M. oryzae* generates a specialized structure called an appressorium that attaches to the leaf and builds up osmotic pressure to penetrate the outer layers, the highly hydrophobic cuticle, and a polysaccharide-rich cell wall (23, 24). During appressorium formation, *M. oryzae* up-regulates a gene (MGG_06069) that encodes a putative PMO (*MoPMO9A* or alternatively named *MoAA9A* or *MoAA91*) (25–28). Of the sixteen putative PMOs present in *M. oryzae*, *MoPMO9A* is the only one expressed at higher levels at this stage of infection, peaking at 4 to 8 h after appressorium induction. This increase in *MoPMO9A* expression is observed with infection in rice and barley and during appressorium formation on an artificial inductive surface (25–28).

Most PMOs have an architecture composed of a single catalytic domain or a catalytic domain followed by an additional C-terminal carbohydrate-binding module (CBM) (5). CBMs have been shown to increase substrate affinity and have also been used to predict PMO substrates (29). The *MoPMO9A* catalytic domain is predicted to be cellulose active; however, it is fused to a chitin-binding CBM. This mismatch is conserved in several fungal plant pathogen PMOs and suggests an important functional role. Indeed, *MoPMO9A*-knockout

Significance

Blast disease is a worldwide concern affecting crops like rice and wheat. During plant penetration, the causative fungus *Magnaporthe oryzae* secretes a polysaccharide monooxygenase (*MoPMO9A*). Here, we show that *MoPMO9A* is active on (1→3, 1→4)- β -glucans present in the cell wall of cereal-type plants, hydroxylating the C4 position of the glycosidic bond and using either oxygen or hydrogen peroxide as a cosubstrate. This PMO has a second domain of unknown function that is highly conserved within a subset of PMOs and is essential for PMO activity. Moreover, *MoPMO9A* deletion results in reduced pathogenicity in rice. Taken together, this work provides insight into the biochemistry of *MoPMO9A* and the domain architecture of PMOs, supporting its role in polysaccharide degradation during plant infection.

Author contributions: A.M.-D., X.Y., T.C.D., R.I.S., W.C.T., N.J.T., and M.A.M. designed research; A.M.-D., X.Y., T.C.D., R.I.S., and W.C.T. performed research; A.M.-D., X.Y., T.C.D., R.I.S., W.C.T., N.J.T., and M.A.M. analyzed data; and A.M.-D. wrote the paper.

Reviewers: J.M.B., The Pennsylvania State University; J.W.K., University of British Columbia; and B.G.M., Florida State University.

The authors declare no competing interest.

Copyright © 2023 the Author(s). Published by PNAS. This article is distributed under [Creative Commons Attribution-NonCommercial-NoDerivatives License 4.0 \(CC BY-NC-ND\)](#).

¹Present address: Department of Pharmaceutical Chemistry, University of California, San Francisco, CA 94158.

²To whom correspondence may be addressed. Email: marletta@berkeley.edu.

This article contains supporting information online at <https://www.pnas.org/lookup/suppl/doi:10.1073/pnas.2215426120/-DCSupplemental>.

Published February 15, 2023.

fungi penetrate less and generate smaller lesions in rice leaves than the wild type (26). It was also shown that the *MoPMO9A* CBM binds to chitin (26). Nevertheless, nothing is known about the role of the catalytic domain or the biological significance of this mismatched architecture.

We hypothesized that after *MoPMO9A* secretion, the CBM binds to fungal cell wall chitin, while the oxidative activity from the catalytic domain weakens the plant cell wall to facilitate pathogen invasion. Herein, we report biochemical insight into *MoPMO9A* structure and catalytic activity that supports this hypothesis and contributes to our understanding of the significance of this mismatched multidomain architecture. Furthermore, we provide evidence that this group of PMOs contains a unique domain of unknown function (DUF) that is required for protein stability and/or catalysis and that is absent in other PMOs of the same family. Finally, we show that *MoPMO9A* is highly expressed during the early stages of plant infection, and its deletion results in reduced pathogenicity in a rice leaf drop assay. A gene ontology (GO) analysis highlights the role of *MoPMO9A* in chitin binding and carbohydrate metabolism consistent with the proposed function in pathogenesis.

Results

MoPMO9A Domain Architecture. The Carbohydrate-Active Enzymes (CAZy) database classifies PMOs into seven auxiliary activity (AA) families based on protein sequence (5, 30). *MoPMO9A* belongs to the AA9 family, which is the family that comprises Pfam03443 and is predicted to act on cellulose. Using Pfam03443 as the input, a sequence similarity network (SSN) was generated with an alignment score of 60 (approximately 40% sequence ID) (Fig. 1A and Dataset S1). SSNs group proteins into clusters based on sequence similarity. *MoPMO9A* belongs to the sixth largest cluster (232 sequences), and the closely grouped node structure denotes a high level of conservation. A detailed analysis of the different architectures found in the *MoPMO9A*-containing cluster revealed that 30% of the sequences, including *MoPMO9A*, have mismatched domains with a catalytic domain predicted to be active on cellulose and a chitin-binding type 1 domain at the C terminus (Fig. 1B). In 220 of the 223 sequences of the *MoPMO9A*-containing cluster, there is a highly conserved region (~80 amino acids) located ~20 amino acids after the catalytic domain (Fig. 1B). This DUF was neither identified using the online SMART tool (31) nor annotated

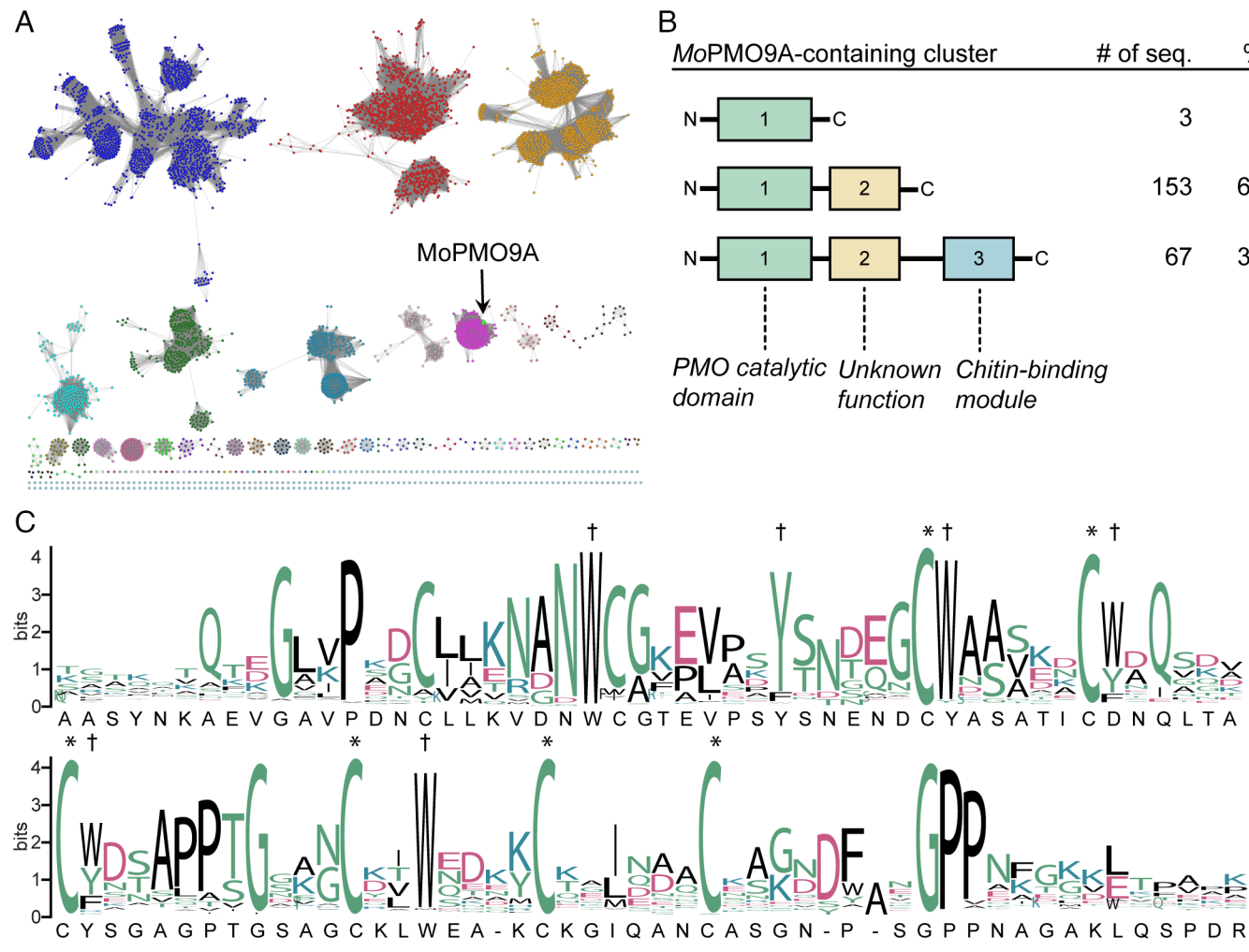


Fig. 1. *MoPMO9A* sequence and domain analysis. (A) A SSN of 5,593 PMOs in the AA9 family was generated using the EFI-EST website with an alignment score of 60. The clusters of sequences are displayed in different colors. The *MoPMO9A*-containing cluster is magenta colored, and the *MoPMO9A* node is highlighted in green. (B) Domain architectures in the *MoPMO9A*-containing cluster. Sequences were aligned using Clustal Omega and visualized with Jalview for sequence length determination. InterPro was used to identify domains 1 and 3. Domain 2 is unannotated and of unknown function. (C) The alignment from B was used to make a sequence logo of domain 2 using the WebLogo website. Residues are colored by their side chain characteristics. The *MoPMO9A* sequence is also displayed. *represents absolutely conserved cysteines, and †represents highly conserved aromatic residues.

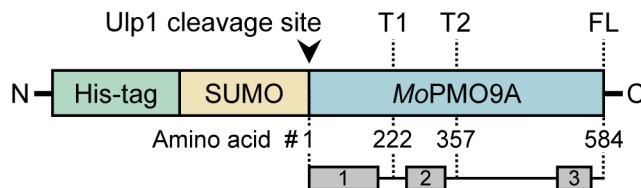


Fig. 2. Representation of pSUMO-MoPMO9A constructs (T1, T2, and FL). The N-terminal tag is removed by Ulp1 to generate MoPMO9A with an N-terminal histidine. The amino acid length of each construct is indicated. Purification details are in *SI Appendix*, Fig. S1. MoPMO9A predicted domains are shown in gray. 1: PMO catalytic domain (AAs 1 to 210); 2: DUF (AAs 243 to 322); 3: chitin-binding domain (AAs 484 to 537).

as a known DUF within the Pfam database (32). Further analysis of this region shows that it contains six absolutely conserved cysteines (C272, C279, C286, C298, C305, and C312) and two more that are present in most of the sequences (Fig. 1C). In addition, there are several conserved aromatic residues: W258, Y266, Y273, D280 (which corresponds to W, Y, or F in other sequences), Y287, and W301. As will be discussed later, these residues could have a role in protein binding to polysaccharides.

MoPMO9A Activity on (1→3, 1→4)- β -Glucans from the Poaceae Family

Family. Two truncations (T1 and T2) and the full-length protein (FL) were cloned and heterologously expressed in *Escherichia coli* (Fig. 2 and *SI Appendix*, Fig. S1A). T1 contains only the PMO catalytic domain, and T2 contains both the catalytic domain and the DUF. In all cases, the protein of interest was expressed in-frame with a hexahistidine tag and a SUMO protein, which were removed leaving no scar with the protease Ulp1 (33). This is essential for PMOs because the N-terminal histidine serves as a bidentate ligand for the active site Cu (34). Consistent with previous PMOs (34), each of the three constructs bound

approximately one equivalent of Cu. Other contaminating metals were not detectable (*SI Appendix*, Fig. S1B and C).

AA9 PMOs are predicted to act on cellulose. However, no activity was observed on Avicel (high-purity cellulose) or a more water-soluble derivative, phosphoric acid-swollen cellulose (PASC), even in the presence of high concentrations of enzyme (Fig. 3A and *SI Appendix*, Fig. S2A). By contrast, cellulose-derived soluble oligosaccharides were detected in a positive control for cellulose degradation using the previously characterized PMO *MtPMO9E* (35). In a search for substrates, assays were carried out with an extended panel of polysaccharides (*SI Appendix*, Table S1). We found that MoPMO9A is active on the water-soluble polysaccharide mixed (1→3, 1→4)- β -D-glucan (MBG) as shown by the change in the HPAEC-PAD elution profile in the presence of enzyme (Fig. 3B and *SI Appendix*, Fig. S2B). The appearance of new peaks coupled with the broadening and shifting of the parent peak, indicative of a more polydisperse polymer, indicates the presence of smaller MBG fragments (Fig. 3C). All of the other polysaccharides tested for activity were inactive. There could, of course, be other substrates among the very broad class of polysaccharides.

MBGs are present in the cell wall of certain lichen and plant species from the graminoid clade of the Poales (grasses and cereals), each species having a specific proportion of β -(1→3) and β -(1→4) bonds (36). In cereals, MBGs are composed predominantly of celotriosyl (degree of polymerization of three glucose units, DP3) and cellotetraosyl (DP4) blocks separated by a single β -(1→3) bond, although celodextrin segments of up to ten to twelve glucose units are present at lower frequencies (37). In contrast, lichenin from Icelandic moss has predominantly β -(1→3) linked celotriosyl units and almost no DP4 segments (38). MoPMO9A was active on MBGs from oats and barley (which are part of the Poaceae family of grasses and cereals), but it was not active on lichenin (*SI Appendix*, Fig. S3).

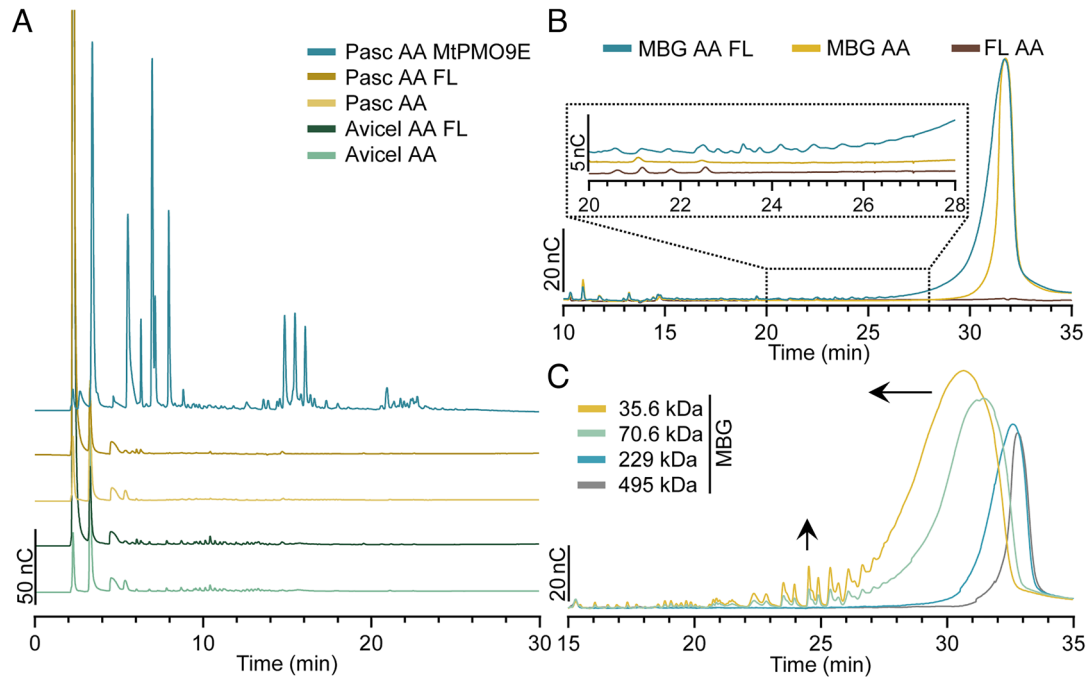


Fig. 3. MoPMO9A activity on β -glucans. (A and B) Representative HPAEC-PAD traces of FL (10 to 20 μ M) activity assays on different polysaccharides (10 to 20 mg/mL in 50 mM MOPS, pH 7, and 50 mM NaCl at 40 °C for 2 h). The y-axis is amperometric signal intensity. Ascorbic acid (AA, 1 mM) was used as a reductant and *MtPMO9E* (5 μ M) as a positive control. PMO action on MBG causes the polydisperse polymer peak to shift to the left and peaks indicative of oxidation to increase. (C) MBG molecular weight standards (10 mg/mL) in 50 mM MOPS, pH 7, and 50 mM NaCl were incubated at 40 °C for 2 h and analyzed by HPAEC-PAD. The arrows indicate the direction of change.

We next compared the activity of the different constructs (T1, T2, and FL). In the absence of a substrate, PMOs reduce O_2 to hydrogen peroxide (H_2O_2), representing another assay to evaluate PMO functionality (39). The T1 construct produced less H_2O_2 and degraded during the incubation (Fig. 4A and *SI Appendix*, Fig. S4). It was also less active on barley MBG compared to the T2 and the FL. This suggests that the DUF is important for the activity and/or the stability of *MoPMO9A*. There were no significant differences between the T2 and FL (Fig. 4).

Regioselectivity of *MoPMO9A*. PMOs can be grouped into three classes based on the regiospecificity of hydroxylation. Those grouped into the PMO-1 and PMO-2 categories hydroxylate at the C1 or C4 position, respectively. Those in the PMO-3 grouping are less regiospecific and hydroxylate at either position. Hydroxylation at C1 or C4 leads to cleavage of the polysaccharide chain, but only the reaction at C4 produces a new reducing end (Fig. 5A). Taking advantage of this difference, the *MoPMO9A* reaction products were analyzed using a 3,5-dinitrosalicylic acid (DNS) colorimetric assay to quantify reducing sugars (40). *MoPMO9A*-derived products from MBGs produced an increase in absorbance in the DNS assay, consistent with a C4-oxidizing PMO (Fig. 5B). Additionally, the retention times of *MoPMO9A*-generated products are in the region where C4 hydroxylated products elute based on data with MBGs treated with a known C4-oxidizing PMO, *MtPMO9E* (35) (*SI Appendix*, Fig. S5). Several studies showed a relationship between PMO sequence and regioselectivity, where C4-oxidizing PMOs have a shorter L2 loop, a longer L3 loop, and an SHK motif near the second histidine in the active site (41–43). The presence of an aspartate (D80) next to the Cu in the active site has also been observed in other C4-oxidizing PMOs (44, 45). Comparison of *MoPMO9A* L2 and L3 loops with other characterized PMOs further supports *MoPMO9A* as a C4-oxidizing PMO (Fig. 5C and *SI Appendix*, Table S2).

The mechanism of PMO action is not completely understood but involves the active site mononuclear Cu center, reducing equivalents, and the use of O_2 or H_2O_2 as a cosubstrate to generate an oxidant capable of O-atom insertion into a nonactivated C-H bond (34, 35) (*SI Appendix*, Fig. S6A). *MoPMO9A* can use either O_2 or H_2O_2 as a cosubstrate (*SI Appendix*, Fig. S6B). Both cosubstrates could be physiological in the context of plant infection as will be discussed later.

MBGs and other polysaccharides are susceptible to oxidation and cleavage by free Cu in the presence of reducing agents, likely by

Fenton-like chemistry which produces •OH (46–49). It has been shown that brown rot fungi utilize a similar mechanism to cleave glycosidic bonds and process biomass (50). To better understand if the observed MBG cleavage in the presence of PMO was due to •OH, uric acid (UA) was added as a scavenger (51, 52). In contrast to what was seen for free Cu, the addition of UA to the PMO reaction had no effect on the activity (*SI Appendix*, Fig. S6 A and C).

MoPMO9A Structural Analysis. The active site of PMOs bind a mononuclear Cu ion through a unique histidine brace motif that requires an N-terminal histidine (34). The EPR spectrum of T2 is diagnostic of a type 2 Cu site ($g_1 = 2.27$, $g_2 = 2.08$, and $g_3 = 2.03$) (53). This site is overall more rhombic than other type 2 Cu sites as observed by the splitting of g_2 and g_3 , consistent with EPR data for other AA9 enzymes (Fig. 6A and *SI Appendix*, Table S3). This result supports the presence of Cu bound to a histidine brace motif in *MoPMO9A*. Indeed, experiments carried out using T2 variants in the active site (H1A, H83A, or H1A/H83A) (*SI Appendix*, Fig. S7) show that both H1 and H83 are required for O_2 reduction and PMO activity on barley MBG (Fig. 6 C and D). The loss of activity cannot be attributed to loss of the active site Cu as both H1A and H83A variants still bound Cu in an equimolar ratio (Fig. 6B).

To better understand the role of the DUF, a 3D structure prediction of *MoPMO9A* using AlphaFold2 was carried out (54). Positions of the residues in the PMO catalytic domain and the DUF are predicted with high confidence, but these domains are linked by a loop predicted with low confidence that may be disordered (Fig. 7A) (55). The PMO catalytic domain has a globular β-sandwich fold, a histidine brace motif (H1 and H83), and secondary sphere amino acids (Y167, Q165, and H157) that are important for catalysis in other PMOs (34, 56) (Fig. 7B). The DUF has a predicted coiled-coil motif made up of two α-helices zippered together by six highly conserved cysteines that form three disulfides (Fig. 7C). The putative disulfides (C286 to C298, C279 to C305, and C272 to C312) are spaced exactly 7 amino acids apart, which corresponds to two α-helix turns. *MoPMO9A*-T2 contains 14 cysteine residues. Mass determination of T2 by intact protein mass spectrometry resulted in a main peak of 37,299 Da, which corresponds to a protein with either 12 cysteines participating as disulfides or, alternatively, all 14 cysteines in disulfides and two deamidations (*SI Appendix*, Fig. S8). T2 has two asparagine residues which are followed by a glycine. These asparagine residues are susceptible to deamidation, which is a common modification found in mass spectrometry analysis (57). This result

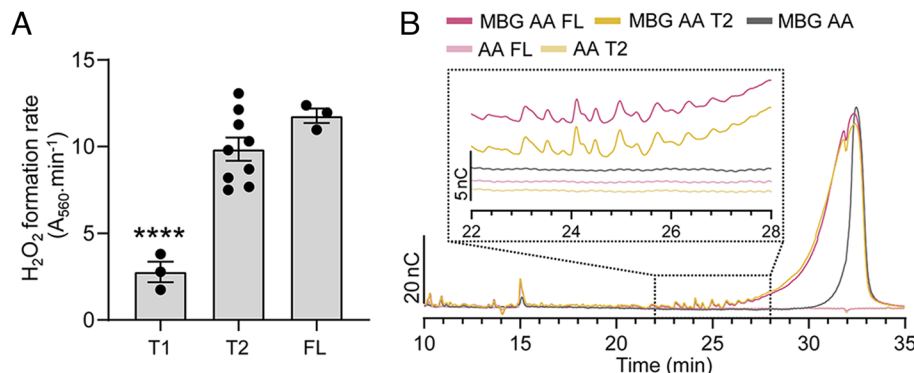


Fig. 4. Characterization of *MoPMO9A* catalytic activity. (A) Hydrogen peroxide formation by *MoPMO9A* constructs was evaluated (no polysaccharide cosubstrate). PMO (1 μ M), HRP (1.3 μ M), Amplex Red (100 μ M), and ascorbic acid (AA, 1 mM) were mixed in 50 mM MOPS, pH 7, and 50 mM NaCl for 30 min, and the conversion of Amplex Red to resorufin was monitored at 560 nm. Bars represent the mean \pm SEM of independent experiments (filled circles). Asterisks denote statistical difference with FL, **** $P < 0.0001$, one-way ANOVA followed by Tukey's test. (B) FL and T2 (20 μ M) were incubated at 40 °C for 2 h with barley MBG (10 mg/mL) and ascorbic acid (AA, 1 mM) in 50 mM MOPS, pH 7, and 50 mM NaCl, and the reaction products were analyzed by HPAEC-PAD. The y-axis is the amperometric signal intensity.

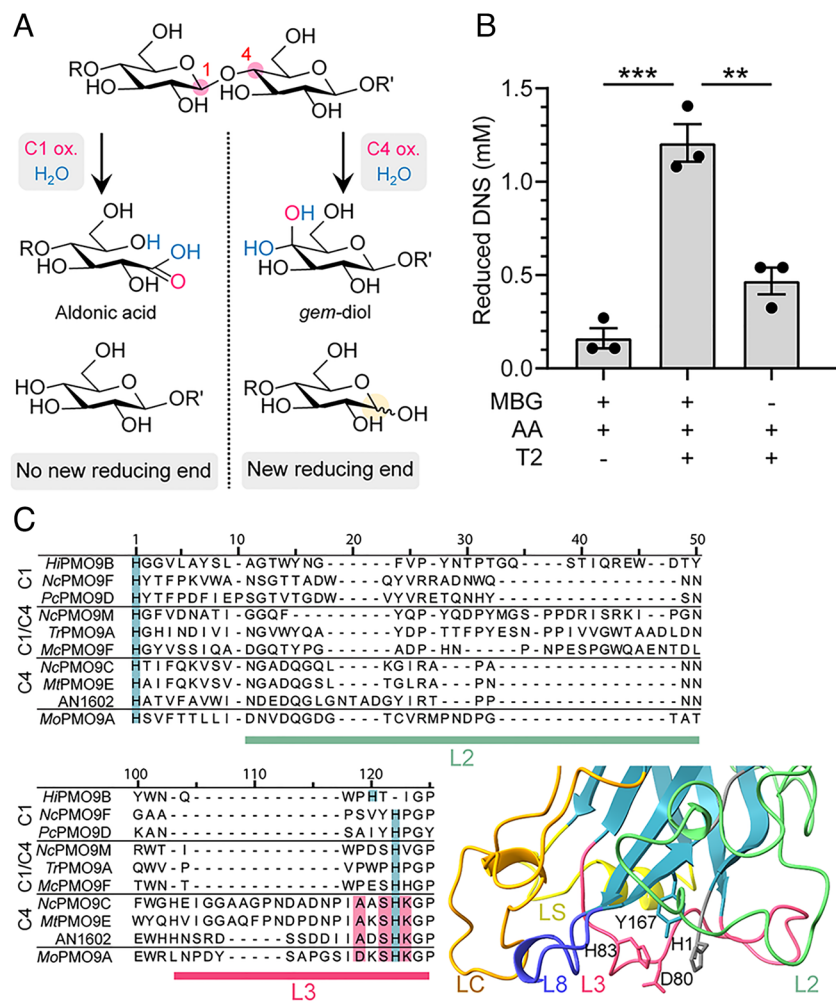


Fig. 5. Regioselectivity of MoPMO9A. (A) C1 or C4 hydroxylation (indicated by a red circle) and subsequent spontaneous hydrolysis (blue) results in different products. The new anomeric carbon is highlighted in yellow. (B) T2 (150 μM), barley MBG (10 mg/mL), and/or ascorbic acid (AA, 2 mM) were incubated in 50 mM MOPS, pH 7, and 50 mM NaCl for 2 h at 40 °C. Reducing ends were quantified by DNS reduction. Bars represent the mean ± SEM of independent samples (filled circles). Asterisks denote statistical difference between means, **P < 0.01, ***P < 0.001, one-way ANOVA followed by Tukey's test. (C) A MSA of MoPMO9A with 47 characterized C1, C4, or C1/C4-oxidizing PMOs from the AA9 family (only 9 sequences shown). A predicted structure of the MoPMO9A catalytic domain using AlphaFold2 is shown. Residues and loops known to be important for regioselectivity in other PMOs are shown in green (loop 2) and pink (loop 3). Other loops are highlighted in blue, orange, and yellow. H1 and H83 align with the histidine brace and are highlighted in blue in the MSA.

supports the AlphaFold2 prediction of all cysteines participating in disulfides. Also of interest, three aromatic/polar residues (Y287, D280, and Y273) spaced ~10 Å apart are positioned on one side of the coiled coil facing the solvent forming a flat surface.

To better characterize the overall structure of the T2 construct, size exclusion chromatography-coupled small-angle X-ray scattering (SEC-SAXS) was carried out, which provides information about size, shape, and oligomeric state of a protein in solution. The T2 construct eluted as a small population of larger oligomers followed by a main peak. The principal component had a radius of gyration (R_g) of 29.3 ± 0.1 Å, likely reflecting a monomeric protein (Fig. 7D). A pair-distance distribution function was calculated for the primary scattering component, and the maximum interelectron distance (D_{\max}) was estimated to be 101 Å (Fig. 7E). The AlphaFold2 predicted structure was calculated to have an R_g of only 22.2 Å and $D_{\max} = 73$ Å, significantly smaller than the experimentally determined scattering. When displayed as Kratky profiles to emphasize mid- q features, the experimental and simulated scattering do not closely overlay ($\chi^2 = 87$). Together, the experimental scattering and pair-distance distribution profile suggest a more expanded protein conformation than predicted by AlphaFold2.

MoPMO9A in Plant Infection. *MoPMO9A* is differentially expressed during the early stages of plant infection and localizes to germinating conidia and appressoria (Fig. 8 A and B). In a previous transcriptional profiling study, *M. oryzae* gene expression was classified into 10 modules of temporally coexpressed genes (58). *MoPMO9A* is in coexpression module 2 together with many other pathogenicity-related genes, including *ALB1* and *BUF1*, which are important for melanin biosynthesis (59, 60), and *SEP5*, which is required for septin ring formation upon plant infection (61). Chitin binding is significantly enriched in GO molecular function analysis and carbohydrate metabolic process significantly enriched in GO biological process analysis among differentially expressed genes coexpressed with *MoPMO9A* at 8 hpi (Fig. 8C). The deletion of *MoPMO9A* results in significantly reduced pathogenicity of the rice blast fungus *M. oryzae*, and the pathogenicity was rescued by reintroducing *MoPMO9A* into the $\Delta pmo9a$ mutant (Fig. 8D). Finally, the histidine brace variant (H1A/H83A) did not fully complement the pathogenicity of $\Delta pmo9a$ mutant, supporting a role for the PMO catalytic activity in the plant infection process (Fig. 8D).

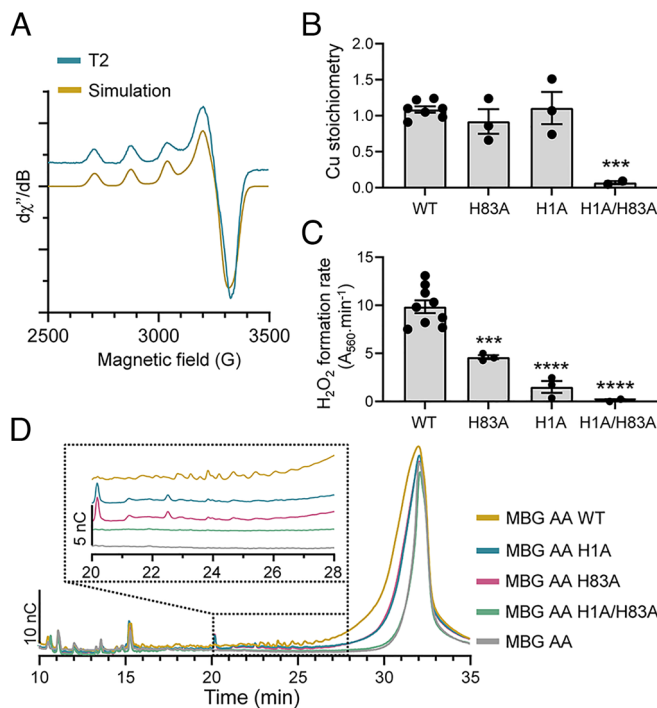


Fig. 6. EPR and mutational analysis of *MoPMO9A*. (A) X-band EPR spectrum of T2 (390 μ M) in 50 mM MOPS, pH 7, and 50 mM NaCl (blue). A simulation is also shown (yellow). Spectra were recorded at 40 K, 9.4 GHz, 0.2 mW power, and 0.5 mT modulation amplitude. Simulation parameters for T2: $g = [2.27\ 2.08\ 2.03]$, $A^{63/65\text{Cu}} = [507\ 5\ 5]$ MHz, and g strain = [0.004 0.06 0.003]. (B) PMO (10 to 100 μ M), BCS (5 mM), and ascorbic acid (AA, 1 mM) in 50 mM MOPS, pH 7, and 50 mM NaCl were incubated at room temperature for 1 h. The copper content was determined by measuring the absorbance of $[\text{Cu}(\text{BCS})_2]^{3-}$ at 483 nm. (C) Hydrogen peroxide formation by the *MoPMO9A* variants was evaluated in the absence of substrate. PMO (1 μ M), HRP (1.3 μ M), Amplex Red (100 μ M), and AA (1 mM) were mixed in 50 mM MOPS, pH 7, and 50 mM NaCl, and the conversion of Amplex Red to resorufin was monitored at 560 nm for 30 min. (B and C) Bars represent the mean \pm SEM of independent experiments (filled circles). Asterisks denote statistical difference with the T2 wild type, *** $P < 0.001$, **** $P < 0.0001$, one-way ANOVA followed by Tukey's test. (D) Different variants of T2 (10 μ M) were incubated with barley MBG (10 mg/mL) and AA (1 mM) in MOPS 50 mM, pH 7, and NaCl 50 mM at 40 °C for 2 h. Representative HPAEC-PAD traces are shown. The y-axis represents the amperometric signal intensity.

Discussion

Since the discovery of PMOs in 2010 (62), several families with different substrate specificities and taxonomic origins have been annotated in the CAZy database (4). In contrast to previously characterized AA9 PMOs, *MoPMO9A* is not active on cellulose but acts on a subset of MBGs (Fig. 3). Whether this catalytic profile is unique for *MoPMO9A* or common for other closely related sequences has not been determined but will be important for proper family classification of this subset of AA9 PMOs.

In the Poaceae family, MBGs appear transiently in growing tissues and accumulate in the endosperm of grain cell walls (63–66). *M. oryzae* is well known to cause rice blast disease. However, this plant pathogen is also known to infect more than 50 different grass species including barley, oats, finger millet, and wheat (67). In fact, there is increasing concern about recent wheat blast outbreaks (68, 69), which are characterized by bleached spikes and loss of grains (70). *M. oryzae* can infect and survive in wheat seeds (71, 72). Given that infectivity studies with a Δ *Mopmo9A*-knockout strain were only carried out on rice plant leaves, and the increasing worldwide threat of wheat blast, it would be important to see whether this phenotype is also observed in a wheat pathogenic strain of the fungus on wheat growing tissues, spikes, and/or

seeds, where MBGs are most abundant. Moreover, since the MBG content varies across different plant species, disease phenotypes using the PMO-knockout strain may vary as well.

The activity profile of *MoPMO9A* on MBGs suggests that the enzyme requires the presence of DP4 blocks or higher. The minimum length of β -(1 \rightarrow 4) sections in the polymer necessary for catalysis has not been determined. The introduction of β -(1 \rightarrow 3) bonds into a β -(1 \rightarrow 4) polymer increases its water solubility and in turn likely increases enzyme access to the substrate (37). It is possible that *MoPMO9A* acts on β -(1 \rightarrow 4) sections of the MBG, requiring the presence of β -(1 \rightarrow 3) bonds either because of binding specificity or increased access to the β -(1 \rightarrow 4) linkage. This may prove to be more general for other AA9 PMOs, like *MtPMO9E* (*SI Appendix*, Fig. S5); however, without chemical standards to quantify the amount of products formed, a direct comparison of activity between different substrates and enzymes is not possible.

Of the 232 sequences that clustered together with *MoPMO9A* in the SSN, 99% also had a highly conserved region that is not present in other clusters (Fig. 1). As of 2021, the Pfam database contains 4244 DUFs, which represent 23% of all Pfam families (32). This conserved region has not been annotated as a DUF, but we named it as such until a function is identified, and it can be renamed accordingly (73). A structure prediction of *MoPMO9A* using AlphaFold2 suggests that the DUF is composed of two α -helices folded as a coiled-coil with three disulfides stabilizing the motif (Fig. 7). It contains three residues (Y287, D280, and Y273) that are spaced ~10 Å from each other and are facing one side of the predicted coiled-coil. Polar and aromatic residues have been shown to participate in carbohydrate binding for PMOs and CBMs (74–76), and this distance corresponds to the length of two β -(1 \rightarrow 4) linked glucose units based on a crystalline cellulose structure, suggesting that the DUF has a role in carbohydrate recognition and binding (77, 78). Further studies, for example, polysaccharide-binding assays and structure–function analysis with specific variants, are necessary to further characterize the function of the DUF. Regarding the orientation of the DUF and the PMO domain, while the AlphaFold2 structure displays an interaction between them, the connecting loop is predicted at low confidence. This region may be a flexible linker between the domains. It is possible that this interdomain tether would allow for independent rigid body-like motion of the domains and that this flexibility accounts for most of the ~30 Å discrepancy in D_{\max} between our experimental SAXS data and the predicted scattering of the AlphaFold2 structure. It is likely that, in solution, the protein takes on a more extended conformation and/or mixture of conformations than that predicted by AlphaFold2 (Fig. 7).

MoPMO9A can utilize H_2O_2 as a cosubstrate similar to other PMOs (*SI Appendix*, Fig. S6) (35, 79, 80). Plants produce H_2O_2 as a response to fungal infections (81). Even though *M. oryzae* secretes effectors to evade this response (20), the presence of nanomolar amounts of H_2O_2 may still be relevant. Enzyme activity with H_2O_2 as a cosubstrate is significantly faster compared to that with O_2 when studied with other PMOs (80). Although the H_2O_2 concentration may be significantly below the K_m of 2.8 μM determined for the PMO CBP21, the faster rate may compensate (80). However, *MoPMO9A* can utilize H_2O_2 only if there is sufficient reducing agent present (*SI Appendix*, Fig. S9).

The results on biological function reproduce and extend previous observations. The higher resolution imaging reported here clearly shows localization of *MoPMO9A* in the wall of the appressorium at 8 hpi. The presence of the PMO at this early stage of infection is consistent with a proposed role in gaining entry into the plant. PMO catalytic activity generally, and *MoPMO9A*

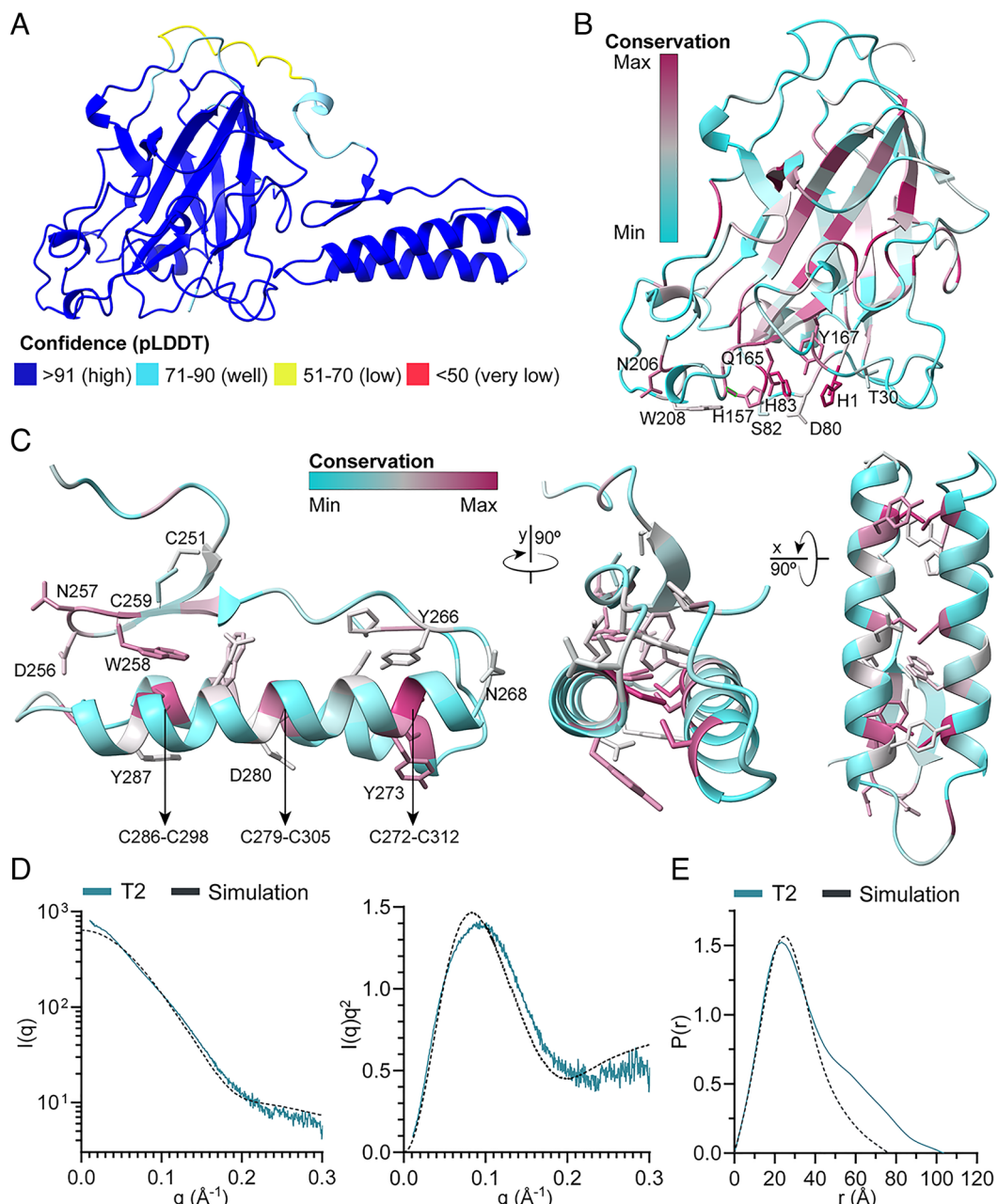


Fig. 7. MoPMO9A-T2 structural analysis. (A) T2 structure prediction using AlphaFold2. Colors represent the per-residue estimate of the prediction confidence (pLDDT). Both domains have a high score and are expected to be modeled with high accuracy. The loop connecting these domains is disordered. (B) T1 AlphaFold2 structure prediction colored by the sequence conservation in *MoPMO9A*-containing cluster using the AL2CO program in ChimeraX. The conservation values range from -1.41 to 2.68. Residues with conservation values higher than half the range in the binding site are highlighted. (C) Three perspectives of the second domain in *MoPMO9A* colored and visualized as in B. The two α -helices are connected by six highly conserved cysteines. (D) SEC-SAXS was performed on the T2 construct (14.3 mg/mL), and the scattering of the main elution peak was determined using evolving factor analysis. The calculated scattering of the AlphaFold2 predicted structure (simulation, dashed lines) is also shown. (E) Pair-distance distribution function ($P(r)$) and D_{\max} were calculated for the experimental (101 Å) and calculated (73.4 Å) SAXS profiles shown in panel D.

specifically, requires an active site copper ion. The copper ion is coordinated through the histidine brace motif (H1 and H83 in *MoPMO9A*), and as shown here, the H1/H83 double mutant is catalytically inactive both toward O_2 reduction to H_2O_2 and MBG hydroxylation. Complementation with this double His variant in the *MoPMO9A* deletion strain does not rescue full virulence as does complementation with the wild-type enzyme, and thus, catalytic activity is required for the full virulence of the rice blast fungus. The most straightforward interpretation of the data overall is that *MoPMO9A* is secreted, attaches to the chitin fungal cell wall, and then, via the activity of the catalytic domain,

cuts into the MBG of the rice leaf, thus gaining entry into the plant host.

It is also possible that adherence of the chitin-binding CBM to the cell wall of the fungus interferes with recognition by plant immune receptors during degradation of the MBG in the rice leaf cell wall. The GO analysis adds further confidence to the proposed role of *MoPMO9A* in infection, given the coexpression with enzymes associated with chitin and carbohydrate metabolism, and fits well with the biochemical results reported here. The appressoria of the H1/H83 variant form normally. No other phenotypes were observed apart from the reduced pathogenicity. While it is possible

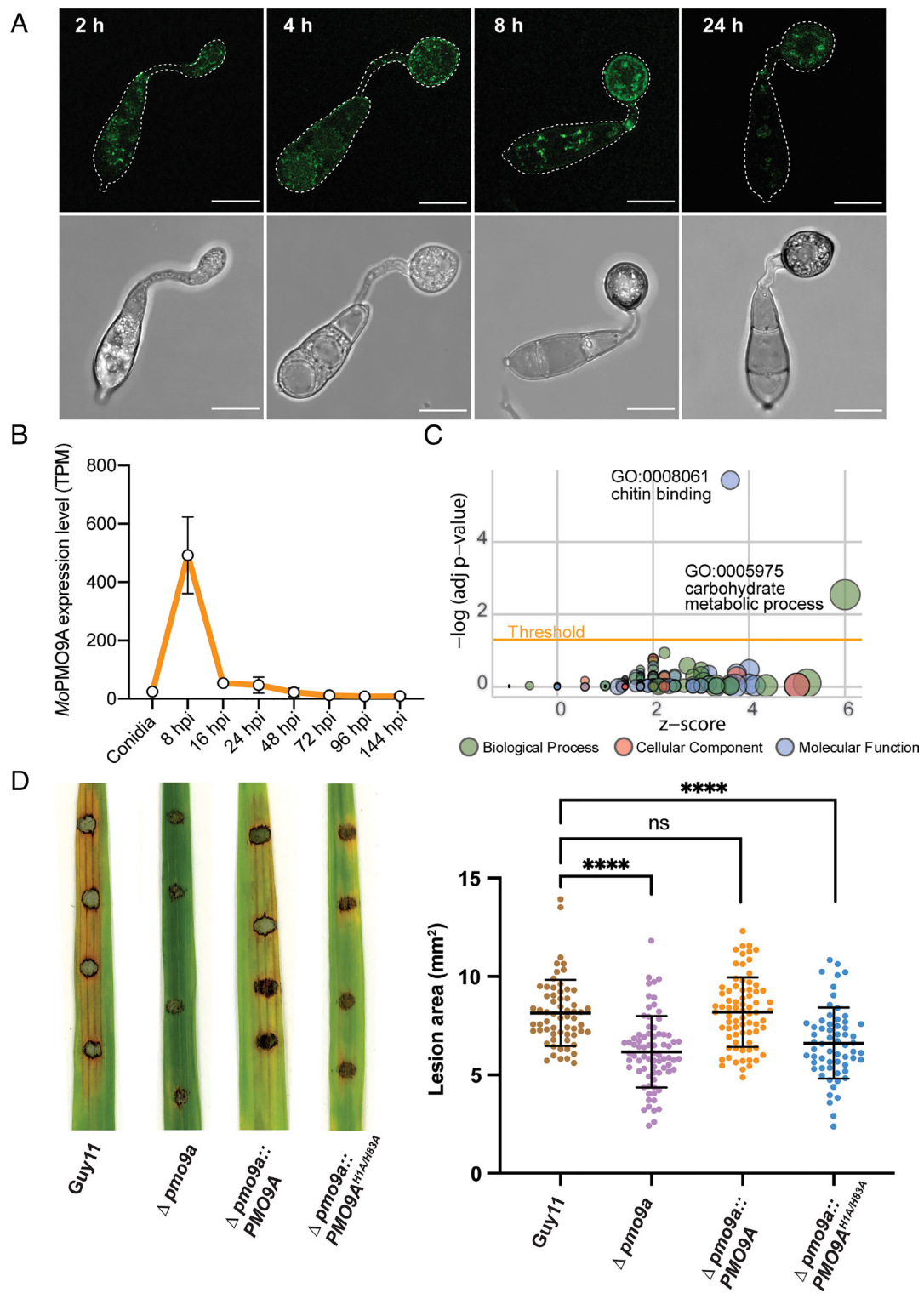


Fig. 8. *MoPMO9A* expression and effect on full virulence of *M. oryzae*. (A) Micrographs showing *MoPMO9A*-GFP localization during appressorium formation. Conidia from strain expressing *MoPMO9A*-GFP were incubated on glass coverslips; images were captured at 2, 4, 8, and 24 h after incubation. (Scale bar, 10 μm .) (B) *MoPMO9A* expression level during plant infection from the RNA-seq of leaf drop infections. Line graph showing the mean TPM value from 3 biological replicates of samples during plant infection (8, 16, 24, 48, 72, 96, and 144 hpi) and two biological replicates from conidial sample. Error bars represent SD. TPM, transcripts per million; hpi, hours postinoculation. (C) GO enrichment analysis of differentially expressed *M. oryzae* genes in the same coexpression module with *MoPMO9A*. Chitin binding is significantly enriched in GO molecular function analysis, while carbohydrate metabolic processes are significantly enriched in GO biological process analysis. (D) Pathogenicity assay of the wild-type strain Guy11, the *PMO9A* gene deletion strain $\Delta pmo9a$, the *PMO9A* gene complement strain $\Delta pmo9a::PMO9A$, and the strain $\Delta pmo9a::PMO9A^{H1A/H83A}$ expressing *MoPMO9A*^{H1A/H83A} in $\Delta pmo9a$ background. Left panel: Representative leaves inoculated with Guy11, $\Delta pmo9a$, $\Delta pmo9a::PMO9A$, and $\Delta pmo9a::PMO9A^{H1A/H83A}$ using leaf drop infection. Right panel: Quantification of the diseased lesion area of Guy11 (62 inoculated leaf drops), $\Delta pmo9a$ (75 inoculated leaf drops), $\Delta pmo9a::PMO9A$ (75 inoculated leaf drops), and $\Delta pmo9a::PMO9A^{H1A/H83A}$ (62 inoculated leaf drops). The midline is the mean disease lesion area observed from all replications of the experiment. Bars represent the mean \pm SD of independent samples (filled circles). Statistical differences between means of Guy11 and $\Delta pmo9a$, Guy11 and $\Delta pmo9a::PMO9A$, and Guy11 and $\Delta pmo9a::PMO9A^{H1A/H83A}$ are indicated as asterisks ($P < 0.0001$) or ns ($P > 0.01$) using the t test with Welch's correction.

that *MoPMO9A* acts on a fungal glucan substrate that contributes to appressorium function, as noted, the double His variant appressoria appear normal.

In conclusion, we have found, in contrast to other AA9 PMOs, that *MoPMO9A* is not active on cellulose but is catalytically active on MBGs from the Poaceae family. *MoPMO9A* hydroxylates the polymer at the C4 position with either O₂ or H₂O₂ as a cosubstrate. The histidine brace motif is required for O₂ reduction, PMO activity on cereal-derived MBGs, and full virulence of the rice blast fungus *M. oryzae*. Bioinformatic analysis led to the identification of a highly conserved DUF that is essential for activity in *MoPMO9A* and may have a role in substrate binding and/or protein stability. Taken together, this work provides fundamental insight into the biochemistry, domain architecture, in vivo expression, and physiological function of *MoPMO9A*, supporting its role in MBG degradation during plant infection.

Materials and Methods

Bioinformatic Analysis of *MoPMO9A* Protein Sequence. Pfam 03443 was the input in the EBI-EST(82) website to generate an SSN comprising 5593 sequences (*Dataset S1*). An alignment score of 60 was used to approximate 40% sequence ID. The clusters of sequences were visualized in Cytoscape (83). Sequences in *MoPMO9A*-containing cluster (232 sequences) were aligned using Clustal Omega (84) and visualized with Jalview (85). Nine sequences without a predicted signal peptide not included. InterPro (86) was used to identify domains 1 (a putative PMO catalytic domain) and 3 (a chitin-binding type 1 domain). Domain 2 is not annotated. Sequences were grouped manually based on their architecture using Jalview. The MSA was then used as an input to make a sequence logo using WebLogo (87). A second MSA was performed using *MoPMO9A* with 47 previously characterized C1-, C4-, or C1/C4-oxidizing PMOs from the AA9 family using Clustal Omega and visualized with Jalview (*SI Appendix, Table S2*).

Cloning, Expression, and Purification of *MoPMO9A* Variants. The full-length gene of *MoPMO9A* (MGG_06069, UniProtKB G4N560) and two truncations containing domain 1 (T1) or domains 1 and 2 (T2) were cloned into the pSUMO vector (a gift from the Marques group) in-frame to the N-terminal hexahistidine tag and the SUMO protein-coding sequence (Fig. 2) (33). See *SI Appendix* for cloning details by PCR and the Gibson assembly (88) (*SI Appendix, Tables S4 and S5*). The signal peptide (amino acids 1 to 19 in the original sequence) was omitted. Site-directed mutagenesis (H1A, H83A, and H1A/H83A) was performed using pSUMO-*MoPMO9A*-T2 plasmid and the Q5 site-directed mutagenesis kit (NEB) using primers detailed in *SI Appendix, Table S4*. All sequences were verified (UC Berkeley Sequencing Facility). In all cases, plasmids were transformed into *Escherichia coli* Rosetta 2 (DE3) plysS competent cells (UC Berkeley MacroLab). Cell cultures were grown in Terrific Broth (TB, RPI) and induced with 0.1 mM isopropyl β-D-1-thiogalactopyranoside (IPTG, Fisher Scientific) for ~18 h at 18 °C, and the protein was purified from the cell lysate using a 5-mL nickel affinity column (HiTrap Chelating, GE). Further details are provided in *SI Appendix*. Fractions with A₂₈₀ higher than 0.1 were dialyzed overnight into 50 mM Tris pH 8, 100 mM NaCl, snap-frozen in liquid nitrogen (with the addition of glycerol to a final concentration of 5%), and stored at -80 °C until further use. Cleavage of tags by Ulp1 protease was performed overnight at RT by adding 0.5 mM dithiothreitol (DTT, Bachem) and Ulp1 in a 1:1,000 ratio. Protein concentrations were determined by the A₂₈₀ and using molar extinction coefficients obtained with Benchling (89) (*SI Appendix, Table S6*). His-tagged Ulp1 was expressed and purified as *MoPMO9A* from *Escherichia coli* Rosetta 2 (DE3) plysS cells transformed with pFGET19_Ulp1 (Addgene plasmid #64697). Fractions containing protein were dialyzed overnight into 50 mM Tris pH 8, 200 mM NaCl, and 5 mM DTT and stored at ~35 μM in the same buffer plus 50% glycerol at -80 °C. Cleaved proteins with a free N-terminal histidine (or alanine in some mutants) were obtained from the flow through of a second Nickel affinity chromatography step. Copper reconstitution was performed by dialysis for 4 h into 50 mM NaOAc pH 5.5 and 10 μM CuSO₄ (Fisher Scientific), and excess copper was removed by dialysis overnight into 20 mM MOPS pH 7 and 20 mM NaCl. Proteins with purities greater than 95% were obtained after a final step of size exclusion chromatography (HiLoad 26/600 Superdex 200 pg or HiLoad 16/600 Superdex 75 pg column, Cytiva) and stored at 4 °C (up to 2 wk) or -20 °C (months). All purification

steps were checked by sodium dodecylsulfate-polyacrylamide gel electrophoresis (SDS-PAGE) using precast stain-free gels (Bio-Rad). Expected molecular weights were predicted using Benchling (89).

Metal Content Measurements. Reconstitution of each variant was determined using the Cu(I)-specific chelator bathocuproinedisulfonic acid (BCS, Sigma) (90). PMO (10 to 100 μM), 5 mM BCS, and 1 mM ascorbic acid (AA, RPI) were incubated in 50 mM MOPS and 50 mM NaCl, pH 7, at room temperature for 1 h. For the T2 truncation, Cu, Fe, Ni, and Zn contents were determined as well by the Inductively Coupled Plasma-Mass Spectrometry (ICP-MS). 10 μM T2 was diluted 1:1 with 4% HNO₃ containing 40 μg/L Ga (Inorganic Ventures) overnight at room temperature in 1.7-mL tubes (Sarstedt). The protein solution was then centrifuged at 20,000 × g for 10 min, and the supernatant was transferred to new tubes (Sarstedt). Samples were analyzed on a Thermo Fisher iCAP Qc ICP mass spectrometer in kinetic energy discrimination mode against a standard curve of known metal concentrations (CMS-5, Inorganic Ventures), with 20 μg/L Ga as an internal standard. Each experiment was carried out in triplicate.

Aerobic Polysaccharide Oxidation Assays. Activity assays contained 10 to 150 μM PMO, 1 to 2 mM AA, and 10 to 20 mg/mL polysaccharide in 50 mM MOPS, pH 7, and 50 mM NaCl. Assays were performed at 25 to 40 °C for 2 h. In negative controls, the PMO, the reducing agent, or the polysaccharide was omitted. *MtPMO9E* (5 μM) (35) was used as a positive control for cellulose degradation. Besides PASC, the polysaccharides used in this work were commercially obtained (*SI Appendix, Table S1*). PASC was prepared from Avicel PH-101 (Fluka Analytical) as described previously (91). For the •OH scavenging experiments, 100 μM UA (Sigma) was added to the mixture. The reactions were quenched by the addition of 0.2 M NaOH, and all the insoluble material was removed by centrifugation at 20,000 g for 20 min. The products of the reaction (10 μL) were analyzed by HPAEC-PAD as detailed in *SI Appendix*. The effect of the incubation on the different variants was analyzed by SDS-PAGE using precast stain-free gels (Bio-Rad).

Anaerobic Polysaccharide Oxidation Assays. Anaerobic activity assays were performed as above but using H₂O₂ as a cosubstrate instead of O₂ at room temperature and inside an anaerobic glove box ([O₂] < 0.1 ppm, MBRAUN). Solutions used were made anaerobic by aliquoting and equilibrating them in small volumes (≤1 mL) for 24 h with the atmosphere in the glove box. A 1/50 dilution was prepared fresh from an ~9.79 M H₂O₂ (Fisher Scientific), and its concentration quantified by the absorbance at 240 nm ($\epsilon = 43.6 \text{ M}^{-1} \text{ cm}^{-1}$) (92). This stock was brought into the glove box and diluted to 5 mM using O₂-free water. H₂O₂ was added to selected samples in 100 μM increments every 15 min until a final concentration of 500 μM, and then, incubation continued for a total of 2 h. Samples were not exposed to O₂ until after quenching and centrifuging as above. The products of the reaction (10 μL) were analyzed by HPAEC-PAD as detailed in *SI Appendix*.

H₂O₂ Formation by the PMO in the Absence of Polysaccharide Substrate. PMO (1 μM), 1.3 μM horseradish peroxidase (HRP), 100 μM Amplex Red, and 1 mM AA were added to 50 mM MOPS, pH 7, and 50 mM NaCl in a 96-well plate. The conversion of Amplex Red to resorufin was monitored at 560 nm at 30-s intervals for 30 min using a SpectraMax340 spectrophotometer (Molecular Devices) (93). Negative controls were carried out without PMO. The slopes from the linear regions were used to compare the rates between samples.

DNS Reduction Assay. The amount of reducing sugars in the samples was quantified by measuring the 3,5-DNS reduction to 3-amino-5-nitrosalicylic acid spectrophotometrically (40). T2 (150 μM), 10 mg/mL barley MBG, and 2 mM AA were incubated in 50 mM MOPS and 50 mM NaCl, pH 7, for 2 h at 40 °C. Controls were without PMO and without polysaccharide. The products of the assays were diluted 1/10 with DNS reagent, heated at 100 °C for 10 min, cooled to room temperature, and the A₅₅₀ measured with a SpectraMax340 spectrophotometer (Molecular Devices). A calibration curve with glucose (1 to 10 mM) was used to quantify the amount of reduced DNS. The DNS reagent was prepared by mixing 1 g DNS (Sigma), 1.6 g NaOH, and 30 g sodium potassium tartrate in 100 mL water.

Electron Paramagnetic Resonance Spectroscopy. X-band continuous-wave EPR spectra were collected from a T2 sample (390 μM in 50 mM MOPS, pH 7, and 50 mM NaCl) with a Bruker (Billerica, MA) EleXsys E500 spectrometer equipped with a cylindrical TE110-mode resonator (ER4122SHQE), an ESR-900

liquid helium cryostat, and an ITC-5 temperature controller (Oxford Instruments ITC503). The spectra were recorded at 40 K at 9.4 GHz using 5.0 G modulation amplitude. Spectral simulations were performed using EasySpin 5.2.35 within MATLAB 2015a software suite (94).

MoPMO9A Structure Prediction Using AlphaFold2. The sequence of MoPMO9A without its signal peptide [amino acids 1 to 19 by SignalP 6.0 (95) prediction] was used as an input into the Google Colab notebook: <https://github.com/sokrypton/ColabFold> (accessed 7/22/2021) using the code in the AlphaFold2_mmseqs2 notebook. The computation was run using a Google Colab GPU. Each computation was run three times to generate a model. The models were not significantly different, so the first model was used for analysis. The molecular graphics and analyses were performed using UCSF ChimeraX 1.3 (96). Coloring by different levels of confidence was done using the per-residue confidence metric (pLDDT) produced by AlphaFold2 on a scale from 0 to 100 (97). Coloring by conservation was done using the same MSA of MoPMO9A-containing cluster sequences, obtained as detailed above, as an input. The conservation values were calculated using the entropy-based measure method from the AL2CO program (98) included in ChimeraX and automatically assigned to the residues in the structure (range from -1.41 to 2.68).

SEC-SAXS. SEC-SAXS of T2 was collected at the SIBYLS beamline (bl12.3.1) at the Advanced Light Source at the Lawrence Berkeley National Laboratory, Berkeley, California (99, 100). T2 (100 μL of 386 μM) was injected using an Agilent 1290 series HPLC system and eluted to an in-line custom-made SAXS flow cell via a Shodex KW-803 column equilibrated with 20 mM MOPS, pH 7, and 20 mM NaCl buffer at a flow rate of 0.65 mL/min. Scattering was collected and processed as previously described (101, 102). Further data processing and analysis were performed in BioXTAS RAW using established protocols (103). Further details of SAXS data collection, processing, and analysis are provided in *SI Appendix*.

Intact Protein Mass Spectrometry. See *SI Appendix*.

Fungal and Plant Growth Conditions and Transformation of *M. oryzae*.

Fungal strains and rice CO39 plants were maintained as described previously (104). *MoPMO9A*-GFP-expressing strain, *PMO9A* gene deletion strain, gene complementation strain, and *MoPMO9A^{H1A/H83A}* variant strain were generated as detailed in *SI Appendix*. Ten-day-old plate cultures of corresponding *M. oryzae* strains were used to harvest conidia for appressorium development

assays and pathogenicity assays, with a final spore concentration 5×10^4 spores per mL. Spores were inoculated on glass coverslips for appressorium development assays, and infected rice leaves were incubated at 24 °C, 12-h photoperiod, and 90% relative humidity in a closed chamber. Positive vectors were transformed into protoplasts of the wild-type *M. oryzae* strain Guy11, as described previously (105). Data points are individual leaf drops measured for diseased area. A total of 62 to 75 leaf drops were observed. The midline is the mean disease lesion area observed from all replications of the experiment, and the errors bars are the SD.

Live-Cell Imaging of *M. oryzae*. Confocal microscopy was carried out using a Leica SP8 laser confocal microscope. Excitation/emission wavelengths were 488 nm/500 to 530 nm for eGFP. Images were analyzed using Leica software with lightning function and maximum intensity projection and ImageJ (106).

Data Analysis. Data are expressed as mean ± SEM, with each independent experiment showed as a filled circle, unless otherwise stated. One-way ANOVA followed by Tukey's multiple comparisons test or t test with Welch's correction was performed using GraphPad Prism version 9.3.1. $P \leq 0.05$ was considered significant. GO enrichment analysis was carried out using R package "mogo" (<https://github.com/TeamMacLean/mogo>) (58).

Data, Materials, and Software Availability. All study data are included in the article and/or *SI Appendix*.

ACKNOWLEDGMENTS. We thank the Marletta laboratory members for critical reading of the manuscript, D. Brauer for help in analyzing the protein mass spectra, C. Chang and S. Merchant laboratories for the ICP-MS, R. David Britt and CalEPR for the EPR facilities, and D. Rosenberg for help with the SAXS analysis. Support from the NIH project ALS-ENABLE (P30 GM124169) and a High-End Instrumentation Grant S100D018483. A.M.-D. and T.C.D. were supported by the NSF grant CHE-1904540. T.C.D. was also supported by the NSF grant MCB-1818283. R.I.S acknowledges NIH grant F32-GM143897. We thank the Li Chair Fund to W.C.T and The Gatsby Charitable Foundation to N.J.T.

Author affiliations: ^aCalifornia Institute for Quantitative Biosciences, University of California, Berkeley, CA 94720; ^bThe Sainsbury Laboratory, University of East Anglia, Norwich Research Park, Norwich NR4 7UH, UK; ^cDepartment of Chemistry, University of California, Berkeley, CA 94720; and ^dDepartment of Molecular and Cell Biology, University of California, Berkeley, CA 94720

1. W. T. Beeson, C. M. Phillips, J. H. D. Cate, M. A. Marletta, Oxidative cleavage of cellulose by fungal copper-dependent polysaccharide monooxygenases. *J. Am. Chem. Soc.* **134**, 890–892 (2012).
2. G. R. Hemsworth, B. Henrissat, G. J. Davies, P. H. Walton, Discovery and characterization of a new family of lytic polysaccharide monooxygenases. *Nat. Chem. Biol.* **10**, 122–126 (2014).
3. R. D. Finn *et al.*, The Pfam protein families database: Towards a more sustainable future. *Nucleic Acids Res.* **44**, D279–D285 (2016).
4. V. Lombard, H. Golaconda Ramulu, E. Drula, P. M. Coutinho, B. Henrissat, The carbohydrate-active enzymes database (CAZy) in 2013. *Nucleic Acids Res.* **42**, D490–D495 (2014).
5. J. A. Hangasyk, T. C. Detomasi, C. M. Lemon, M. A. Marletta, “Glycosidic bond oxidation: The structure, function, and mechanism of polysaccharide monooxygenases” in *Comprehensive Natural Products III*, (Elsevier, 2020), pp. 298–331.
6. S. T. Coradetti, Y. Xiong, N. L. Glass, Analysis of a conserved cellulase transcriptional regulator reveals inducer-independent production of cellulolytic enzymes in *Neurospora crassa*. *Microbiol. Open* **2**, 595–609 (2013).
7. V. W. Wu *et al.*, The regulatory and transcriptional landscape associated with carbon utilization in a filamentous fungus. *Proc. Natl. Acad. Sci. U.S.A.* **117**, 6003–6013 (2020).
8. P. K. Busk, L. Lange, Classification of fungal and bacterial lytic polysaccharide monooxygenases. *BMC Genom.* **16**, 368 (2015).
9. M. Agostoni, J. A. Hangasyk, M. A. Marletta, Physiological and molecular understanding of bacterial polysaccharide monooxygenases. *Microbiol. Mol. Biol. Rev. MMBR* **81**, e00015–17 (2017).
10. K. S. Johansen, Lytic polysaccharide monooxygenases: The microbial power tool for lignocellulose degradation. *Trends Plant Sci.* **21**, 926–936 (2016).
11. C. Fu, J. Ao, A. Dettmann, S. Seiler, S. J. Free, Characterization of the *Neurospora crassa* cell fusion proteins, HAM-6, HAM-7, HAM-8, HAM-9, HAM-10, AMPH-1 and WHI-2. *PLOS One* **9**, e107773 (2014).
12. F. Sabbadin *et al.*, An ancient family of lytic polysaccharide monooxygenases with roles in arthropod development and biomass digestion. *Nat. Commun.* **9**, 1–12 (2018).
13. R. F. Seipek, M. Kaltenpoth, M. I. Hutchings, *Streptomyces* as symbionts: An emerging and widespread theme? *FEMS Microbiol. Rev.* **36**, 862–876 (2012).
14. D. L. Distel, D. J. Beaujouan, W. Morrill, Coexistence of multiple proteobacterial endosymbionts in the gills of the wood-boring bivalve *Lyrudus pedicellatus* (Bivalvia: Teredinidae). *Appl. Environ. Microbiol.* **68**, 6292–6299 (2002).
15. R. M. O'Connor *et al.*, Gill bacteria enable a novel digestive strategy in a wood-feeding mollusk. *Proc. Natl. Acad. Sci. U.S.A.* **111**, E5096–E5104 (2014).
16. E. Chiu *et al.*, Structural basis for the enhancement of virulence by viral spindles and their in vivo crystallization. *Proc. Natl. Acad. Sci. U.S.A.* **112**, 3973–3978 (2015).
17. R. F. Frederiksen *et al.*, Bacterial chitinases and chitin-binding proteins as virulence factors. *Microbiology* **159**, 833–847 (2013).
18. E. Wong *et al.*, The *Vibrio cholerae* colonization factor GbpA possesses a modular structure that governs binding to different host surfaces. *PLoS Pathog.* **8**, e1002373 (2012).
19. G. Jagadeeswaran, L. Veale, A. J. Mort, Do lytic polysaccharide monooxygenases aid in plant pathogenesis and herbivory? *Trends Plant Sci.* **26**, 142–155 (2021).
20. R. A. Wilson, N. J. Talbot, Under pressure: Investigating the biology of plant infection by *Magnaporthe oryzae*. *Nat. Rev. Microbiol.* **7**, 185–195 (2009).
21. D. O. TeBeest, C. Guerber, M. Ditmore, Rice blast. *UpToDate* (2012). <https://www.apnsnet.org/edcenter/isandpath/fungalsaco/pdlessons/Pages/RiceBlast.aspx>. Accessed 15 January 2022.
22. M. C. Fisher *et al.*, Emerging fungal threats to animal, plant and ecosystem health. *Nature* **484**, 186–194 (2012).
23. Y. Hegde, P. E. Kolattukudy, Cuticular waxes relieve self-inhibition of germination and appressorium formation by the conidia of *Magnaporthe grisea*. *Physiol. Mol. Plant Pathol.* **51**, 75–84 (1997).
24. L. S. Ryder, N. J. Talbot, Regulation of appressorium development in pathogenic fungi. *Curr. Opin. Plant Biol.* **26**, 8–13 (2015).
25. Y. Dong *et al.*, Global genome and transcriptome analyses of *Magnaporthe oryzae* epidemic isolate 98–06 uncover novel effectors and pathogenicity-related genes, revealing gene gain and lose dynamics in genome evolution. *PLOS Pathog.* **11**, e1004801 (2015).
26. Y. Li *et al.*, *Magnaporthe oryzae* auxiliary activity protein MoAa91 functions as chitin-binding protein to induce appressorium formation on artificial inductive surfaces and suppress plant immunity. *mBio* **11**, e03304–19 (2020).
27. D. M. Soanes, A. Chakrabarti, K. H. Paszkiewicz, A. L. Dawe, N. J. Talbot, Genome-wide transcriptional profiling of appressorium development by the rice blast fungus *Magnaporthe oryzae*. *PLoS Pathog.* **8**, e1002514 (2012).
28. M. Shimizu *et al.*, RNA-Seq of *in planta* -expressed *Magnaporthe oryzae* genes identifies *MoSVP* as a highly expressed gene required for pathogenicity at the initial stage of infection. *Mol. Plant Pathol.* **20**, 1682–1695 (2019).
29. V. V. Vu, W. T. Beeson, E. A. Span, E. R. Farquhar, M. A. Marletta, A family of starch-active polysaccharide monooxygenases. *Proc. Natl. Acad. Sci. U.S.A.* **111**, 13822–13827 (2014).

30. A. Levasseur, E. Drula, V. Lombard, P. M. Coutinho, B. Henrissat, Expansion of the enzymatic repertoire of the CAZy database to integrate auxiliary redox enzymes. *Biotechnol. Biofuels* **6**, 41 (2013).
31. I. Letunic, S. Khedkar, P. Bork, SMART: Recent updates, new developments and status in 2020. *Nucleic Acids Res.* **49**, D458–D460 (2021).
32. J. Mistry *et al.*, Pfam: The protein families database in 2021. *Nucleic Acids Res.* **49**, D412–D419 (2021).
33. F. Guerrero, A. Ciragan, H. Iwai, Tandem SUMO fusion vectors for improving soluble protein expression and purification. *Protein Expr. Purif.* **116**, 42–49 (2015).
34. J. A. Hangasyk, T. C. Detomaso, M. A. Marletta, Glycosidic bond hydroxylation by polysaccharide monooxygenases. *Trends Chem.* **1**, 198–209 (2019).
35. J. A. Hangasyk, A. T.avarone, M. A. Marletta, Reactivity of O2 versus H2O2 with polysaccharide monooxygenases. *Proc. Natl. Acad. Sci. U.S.A.* **115**, 4915–4920 (2018).
36. P. J. Wood, J. Weisz, B. A. Blackwell, Molecular characterization of cereal β -D-glucans. Structural analysis of oat β -D-glucan and rapid structural evaluation of β -D-glucans from different sources by high-performance liquid chromatography of oligosaccharides released by lichenase. *Cereal Chem.* **68**, 31–39 (1991).
37. J. Woodward, G. Fincher, B. Stone, Water-soluble (1→3), (1→4)- β -D-glucans from barley (*Hordeum vulgare*) endosperm II. Fine structure. *Carbohydr. Polym.* **3**, 207–225 (1983).
38. S. Tosh, Evaluation of structure in the formation of gels by structurally diverse (1 β)(1 α)-?glucans from four cereal and one lichen species. *Carbohydr. Polym.* **57**, 249–259 (2004).
39. R. Kittl, D. Kracher, D. Burgstaller, D. Haltrich, R. Ludwig, Production of four *Neurospora crassa* lytic polysaccharide monooxygenases in *Pichia pastoris* monitored by a fluorimetric assay. *Biotechnol. Biofuels* **5**, 79 (2012).
40. G. L. Miller, Use of dinitrosalicylic acid reagent for determination of reducing sugar. *Anal. Chem.* **31**, 426–428 (1959).
41. V. V. Vu, W. T. Beeson, C. M. Phillips, J. H. D. Cate, M. A. Marletta, Determinants of regioselective hydroxylation in the fungal polysaccharide monooxygenases. *J. Am. Chem. Soc.* **136**, 562–565 (2014).
42. Z. Forsberg *et al.*, Structural determinants of bacterial lytic polysaccharide monooxygenase functionality. *J. Biol. Chem.* **293**, 1397–1412 (2018).
43. B. Danneels, M. Tanghe, T. Desmet, Structural features on the substrate-binding surface of fungal lytic polysaccharide monooxygenases determine their oxidative regioselectivity. *Biotechnol. J.* **14**, e1800211 (2019).
44. A. S. Borisova *et al.*, Structural and functional characterization of a lytic polysaccharide monooxygenase with broad substrate specificity. *J. Biol. Chem.* **290**, 22955–22969 (2015).
45. M. Wu *et al.*, Crystal structure and computational characterization of the lytic polysaccharide monooxygenase GH61D from the Basidiomycota Fungus *Phanerochaete chrysosporium*. *J. Biol. Chem.* **288**, 12828–12839 (2013).
46. R. Kivelä, "Non-enzymatic degradation of (1→3)(1→4)- β -D-glucan in aqueous processing of oats," Ph.D. thesis, University of Helsinki, Helsinki (2011), p. 22.
47. E. E. Johansson, J. Lind, Free radical mediated cellulose degradation during high consistency ozonation. *J. Wood Chem. Technol.* **25**, 171–186 (2005).
48. P. Paruvuori, A. Hamunen, P. Forssell, K. Autio, K. Poutanen, Oxidation of potato starch by hydrogen peroxide. *Starch – Stärke* **47**, 19–23 (1995).
49. C. Schweikert, A. Liszak, P. Schopfer, Polysaccharide degradation by Fenton reaction- or peroxidase-generated hydroxyl radicals in isolated plant cell walls. *Phytochemistry* **61**, 31–35 (2002).
50. V. Arantes, J. Jellison, B. Goodell, Peculiarities of brown-rot fungi and biochemical Fenton reaction with regard to their potential as a model for bioprocessing biomass. *Appl. Microbiol. Biotechnol.* **94**, 323–338 (2012).
51. T. Masuda, H. Shinohara, M. Kondo, Reactions of hydroxyl radicals with nucleic acid bases and the related compounds in gamma-irradiated aqueous solution. *J. Radiat. Res. (Tokyo)* **16**, 153–161 (1975).
52. V. Demichelis, C. Quijano, B. Alvarez, R. Radi, Inactivation and nitration of human superoxide dismutase (SOD) by fluxes of nitric oxide and superoxide. *Free Radic Biol Med* **42**, 1359–68 (2007).
53. T. Ljones, T. Skotland, *Copper Proteins and Copper Enzymes*, R. Lontie, Ed. (CRC Press, Boca Raton, FL, 1984), p. 131.
54. J. Jumper *et al.*, Highly accurate protein structure prediction with AlphaFold. *Nature* **596**, 583–589 (2021).
55. K. M. Ruff, R. V. Pappu, AlphaFold and implications for intrinsically disordered proteins. *J. Mol. Biol.* **433**, 167208 (2021).
56. E. A. Span, D. L. M. Suess, M. C. Deller, R. D. Britt, M. A. Marletta, The role of the secondary coordination sphere in a fungal polysaccharide monooxygenase. *ACS Chem. Biol.* **12**, 1095–1103 (2017).
57. J. Svozil, K. Baerenfaller, "A cautionary tale on the inclusion of variable posttranslational modifications in database-dependent searches of mass spectrometry data" in *Methods in Enzymology*, (Elsevier, 2017), pp. 433–452.
58. X. Yan, The transcriptional landscape of plant infection by the rice blast fungus *Magnaporthe oryzae* reveals distinct families of temporally co-regulated and structurally conserved effectors. *Plant Biol.* [Preprint] (2022), 10.1101/2022.07.18.500532 (Accessed 8 August 2022).
59. Y. Oh *et al.*, Transcriptome analysis reveals new insight into appressorium formation and function in the rice blast fungus *Magnaporthe oryzae*. *Genome Biol.* **9**, R85 (2008).
60. B. Valent, L. Farrall, F. G. Chumley, Magnaporthe grisea genes for pathogenicity and virulence identified through a series of backcrosses. *Genetics* **127**, 87–101 (1991).
61. Y. F. Dagdas *et al.*, Septin-mediated plant cell invasion by the rice blast fungus *Magnaporthe oryzae*. *Science* **336**, 1590–1595 (2012).
62. G. Vaaje-Kolstad *et al.*, An oxidative enzyme boosting the enzymatic conversion of recalcitrant polysaccharides. *Science* **330**, 219–222 (2010).
63. N. C. Carita, M. C. McCann, The maize mixed-linkage (1→3), (1→4)- β -D-Glucan polysaccharide is synthesized at the golgi membrane. *Plant Physiol.* **153**, 1362–1371 (2010).
64. R. A. Burton, G. B. Fincher, Current challenges in cell wall biology in the cereals and grasses. *Front. Plant Sci.* **3**, 130 (2012).
65. A. K. Jason, L. M. Trethewey, P. J. Campbell, Harris, (1→3), (1→4)- β -D-Glucans in the cell walls of the poales (Sensu Lato): An immunogold labeling study using a monoclonal antibody. *Am. J. Bot.* **92**, 1660–1674 (2005).
66. R. C. Brown, B. E. Lemmon, B. A. Stone, O.-A. Olsen, Cell wall (1→3)- and (1→3, 1→4)- β -glucans during early grain development in rice (*Oryza sativa* L.). *Planta* **202**, 414–426 (1997).
67. N. Cruz-Mireles, A. B. Eseola, M. Osés-Ruiz, L. S. Ryder, N. J. Talbot, From appressorium to transpressorium—Defining the morphogenetic basis of host cell invasion by the rice blast fungus. *PLOS Pathog.* **17**, e1009779 (2021).
68. M. T. Islam *et al.*, Emergence of wheat blast in Bangladesh was caused by a South American lineage of *Magnaporthe* oryzae. *BMC Biol.* **14**, 84 (2016).
69. B. Tembo *et al.*, Detection and characterization of fungus (*Magnaporthe oryzae* pathotype *Triticum*) causing wheat blast disease on rain-fed grown wheat (*Triticum aestivum* L.) in Zambia. *PLoS One* **15**, e0238724 (2020).
70. S. K. Paul *et al.*, *Oryzae* pathotype of *Magnaporthe oryzae* can cause typical blast disease symptoms on both leaves and spikes of wheat under a growth room condition. *Phytopathol. Res.* **4**, 9 (2022).
71. S. I. Martinez, A. Wegner, S. Bohnert, U. Schaffrath, A. Perello, Tracing seed to seedling transmission of the wheat blast pathogen *Magnaporthe oryzae* pathotype *Triticum*. *Plant Pathol.* **70**, 1562–1571 (2021).
72. C. D. Cruz, B. Valent, Wheat blast disease: Danger on the move. *Trop. Plant Pathol.* **42**, 210–222 (2017).
73. A. Bateman, P. Coggill, R. D. Finn, DUFs: Families in search of function. *Acta Crystallograph. Sect. F Struct. Biol. Cryst. Commun.* **66**, 1148–1152 (2010).
74. G. Courtade, Z. Forsberg, E. B. Heggset, V. G. H. Eijnsink, F. L. Aachmann, The carbohydrate-binding module and linker of a modular lytic polysaccharide monooxygenase promote localized cellulose oxidation. *J. Biol. Chem.* **293**, 13006–13015 (2018).
75. K. E. H. Frandsen *et al.*, The molecular basis of polysaccharide cleavage by lytic polysaccharide monooxygenases. *Nat. Chem. Biol.* **12**, 298–303 (2016).
76. G. Courtade *et al.*, Interactions of a fungal lytic polysaccharide monooxygenase with β -glucan substrates and cellobiose dehydrogenase. *Proc. Natl. Acad. Sci. U.S.A.* **113**, 5922–5927 (2016).
77. Y. Nishiyama, P. Langan, H. Chanzy, Crystal structure and hydrogen-bonding system in cellulose I β from synchrotron X-ray and neutron fiber diffraction. *J. Am. Chem. Soc.* **124**, 9074–9082 (2002).
78. X. Li, W. T. Beeson, C. M. Phillips, M. A. Marletta, J. H. D. Cate, Structural basis for substrate targeting and catalysis by fungal polysaccharide monooxygenases. *Struct. Lond. Engl.* **1993**, 1051–1061 (2012).
79. B. Bissaro *et al.*, Oxidative cleavage of polysaccharides by monocupper enzymes depends on H2O2. *Nat. Chem. Biol.* **13**, 1123–1128 (2017).
80. S. Kuusk *et al.*, Kinetics of H2O2-driven degradation of chitin by a bacterial lytic polysaccharide monooxygenase. *J. Biol. Chem.* **293**, 523–531 (2018).
81. H. Kaku *et al.*, Plant cells recognize chitin fragments for defense signaling through a plasma membrane receptor. *Proc. Natl. Acad. Sci. U.S.A.* **103**, 11086–11091 (2006).
82. J. A. Gerlt *et al.*, Enzyme function initiative-enzyme similarity tool (EFI-EST): A web tool for generating protein sequence similarity networks. *Biochim. Biophys. Acta* **1854**, 1019–1037 (2015).
83. P. Shannon *et al.*, Cytoscape: A software environment for integrated models of biomolecular interaction networks. *Genome. Res.* **13**, 2498–2504 (2003).
84. F. Sievers *et al.*, Fast, scalable generation of high-quality protein multiple sequence alignments using Clustal Omega. *Mol. Syst. Biol.* **7**, 539 (2011).
85. A. M. Waterhouse, J. B. Procter, D. M. A. Martin, M. Clamp, G. J. Barton, Jalview Version 2—a multiple sequence alignment editor and analysis workbench. *Bioinformatics* **25**, 1189–1191 (2009).
86. M. Blum *et al.*, The InterPro protein families and domains database: 20 years on. *Nucleic Acids Res.* **49**, D344–D354 (2021).
87. G. E. Crooks, G. Hon, J.-M. Chandonia, S. E. Brenner, WebLogo: A sequence logo generator: Figure 1. *Genome. Res.* **14**, 1188–1190 (2004).
88. D. G. Gibson *et al.*, Enzymatic assembly of DNA molecules up to several hundred kilobases. *Nat. Methods* **6**, 343–345 (2009).
89. Benchling Biology Software. <https://benchling.com>. Accessed 15 September 2020.
90. A. Badarau, C. Dennison, Copper trafficking mechanism of CXXC-containing domains: Insight from the pH-dependence of their Cu(II) affinities. *J. Am. Chem. Soc.* **133**, 2983–2988 (2011).
91. Y.-H.P. Zhang, J. Cui, L. R. Lynd, L. R. Kuang, A transition from cellulose swelling to cellulose dissolution by α -Phosphoric acid: evidence from enzymatic hydrolysis and supramolecular structure. *Biomacromolecules* **7**, 644–648 (2006).
92. R. W. Noble, Q. H. Gibson, The reaction of ferrous horseradish peroxidase with hydrogen peroxide. *J. Biol. Chem.* **245**, 2409–2413 (1970).
93. V. V. Vu *et al.*, Substrate selectivity in starch polysaccharide monooxygenases. *J. Biol. Chem.* **294**, 12157–12166 (2019).
94. S. Stoll, A. Schweiger, EasySpin, a comprehensive software package for spectral simulation and analysis in EPR. *J. Magn. Reson.* **178**, 42–55 (2006).
95. F. Teufel, SignalP 6.0 predicts all five types of signal peptides using protein language models. *Nat. Biotechnol. [Preprint]* (2022), 10.1038/s41587-021-01156-3 (Accessed 6 April 2022).
96. E. F. Petersen *et al.*, UCSF CHIMERA-X: Structure visualization for researchers, educators, and developers. *Protein. Sci.* **30**, 70–82 (2021).
97. K. Tunyasuvunakool *et al.*, Highly accurate protein structure prediction for the human proteome. *Nature* **596**, 590–596 (2021).
98. J. Pei, N. V. Grishin, AL2CO: Calculation of positional conservation in a protein sequence alignment. *Bioinformatics* **17**, 700–712 (2001).
99. S. Classen *et al.*, Software for the high-throughput collection of SAXS data using an enhanced Blu-Ice / DC5 control system. *J. Synchrotron Radiat.* **17**, 774–781 (2010).
100. S. Classen *et al.*, Implementation and performance of SIBYLS: A dual endstation small-angle X-ray scattering and macromolecular crystallography beamline at the Advanced Light Source. *J. Appl. Crystallogr.* **46**, 1–13 (2013).
101. K. N. Dyer *et al.*, High-throughput SAXS for the characterization of biomolecules in solution: A practical approach. *Methods Mol. Biol.* **1091**, 245–258 (2014).
102. G. L. Hura *et al.*, Robust, high-throughput solution structural analyses by small angle X-ray scattering (SAXS). *Nat. Methods* **6**, 606–612 (2009).
103. J. B. Hopkins, R. E. Gillilan, S. Skou, BioXTAS RAW: Improvements to a free open-source program for small-angle X-ray scattering data reduction and analysis. *J. Appl. Crystallogr.* **50**, 1545–1553 (2017).
104. N. J. Talbot, Y. P. Salch, M. Ma, J. E. Hamer, Karyotypic variation within clonal lineages of the rice blast fungus, *Magnaporthe grisea*. *Appl. Environ. Microbiol.* **59**, 585–593 (1993).
105. N. J. Talbot, D. J. Ebbole, J. E. Hamer, Identification and characterization of MPG1, a gene involved in pathogenicity from the rice blast fungus *Magnaporthe grisea*. *Plant Cell* **5**, 1575–1590 (1993).
106. C. A. Schneider, W. S. Rasband, K. W. Eliceiri, NIH image to ImageJ: 25 years of image analysis. *Nat. Methods* **9**, 671–675 (2012).